AD-A248 609

Under-Ice Broadband Transient Measurements and Processing

DTIC
ELECTE
MAR 30 1992
S B D

R. W. Meredith
Ocean Acoustics Division
Ocean Acoustics and Technology Directorate

92-07891

Approved for public release; distribution is unlimited. Naval Oceanographic and Atmospheric Research Laboratory, Stennis Space Center, Mississippi 39529-5004.

Foreword

The Arctic Ocean is an acoustically unique region because of low surface temperatures and the presence of the ice canopy. Seasonal variations in ice coverage, thickness, and roughness make the Arctic a dynamic and complex environment in which naval antisubmarine warfare acoustic systems must operate. This research examines horizontal spatial coherence measurements for broadband transients and examines the change in coherence due to a single under-ice reflection dependant on sensor depth and frequency.

W. B. Moseley
Technical Director

L. R. Elliott, Commander, USN
Commanding Officer

Executive Summary

This report examines the horizontal spatial coherence of broadband acoustic energy in the frequency range 100–1200 Hz from explosive sources under the ice pack. The data were recorded on four hydrophone pairs with a nominal sensor separation of 370 m from source ranges from 3 to 25 km. Mean-square coherence is computed separately for the direct and ice-reflected propagation paths, and octave-band frequency averaging reduces variability inherent in the coherence estimation associated with explosive acoustic sources. Coherence varies significantly with sensor depth, range, and frequency. Background noise coherence is also examined briefly. Changes in coherence because of under-ice reflection are smallest for the 100–200 Hz octave band, but the change may be as high as 50% for the higher frequency bands.

Accession For
NTIS
A-1

Acknowledgments

This research was supported by the Office of Naval Technology, Program Element 0602435N. Technical management was provided by Dr. Dan J. Ramsdale, and program management by Dr. E. R. Franchi.

The author is indebted and grateful to Dr. A. E. Leybourne of the University of Southern Mississippi and Ms. Michelle Meitzler of Syntek, Inc. for assistance with programming and data processing.

The mention of commercial products or the use of company names does not in any way imply endorsement by the U.S. Navy or NOARL.

Contents

I. Introduction 1

II. Experiment 1
A. Geometry 1
B. Data Acquisition System 1

III. Data Processing 2
A. Digitizing 2
B. Coherence Estimation 3

IV. Broadband Acoustic Sources 5
A. Underwater Explosives 5
B. Time Series and Spectrum Analysis 6

V. Coherence Estimates 7
A. Direct and Ice-Reflected Arrivals 7
B. Background Noise Coherence 7
C. Horizontal Separation and Spatial Coherence 14

VI. Coherence Change After Reflection 15

VII. Summary 15

VIII. References 19

Under-Ice Broadband Transient Measurements and Processing

I. Introduction

In the last few years, the Naval Oceanographic and Atmospheric Research Laboratory has played a major role in the U.S. Navy program for exploratory development in Arctic environmental acoustics.[1] The naval antisubmarine warfare importance of the Arctic Ocean has increased, and significant manpower has been devoted to measuring and understanding the effects of the Arctic environment on ASW systems.

Under the pack ice, the sound speed profile is reasonably stable, and low-frequency propagation anomalies are caused by interaction with the under-ice surface. Acoustic energy emissions from potential targets have been decreasing, making long-range detections more difficult, even in the low ambient noise regions that can exist under the ice pack. Thus, broadband passive systems may be required to achieve satisfactory signal-to-noise ratios for long-range detection and localization.

This report addresses the effect of under-ice reflection on the horizontal spatial stability of broadband acoustic signals under smooth pack ice. The goal of this study is to estimate broadband coherence and to examine the change in coherence after a single under-ice reflection.

II. Experiment

A. Geometry

The data were collected in fall 1984 during an Arctic field exercise conducted by the U.S. Navy from ice camp Aplis in the Beaufort Sea located approximately 150 nmi north of Barter Island, Alaska. Three vertical receiving arrays (horizontal separation 363 m and 375 m) were suspended to a depth of 300 m (Fig. 1).

The effects of under-ice reflection on horizontal coherence are examined using four pairs of hydrophones, as shown in Figure 1. The hydrophone pairs differ in depth, horizontal separation, and free-field voltage sensitivity. Explosive sound underwater signaling (SUS) charges of 6 oz. TNT-equivalent were detonated periodically along a source track perpendicular to the baseline of the receiving arrays over a range of approximately 2 to 50 nmi. The Mark 123 Mod 0 SUS[2] detonates at 1000 ft ± 100 ft. The sound velocity profile, derived from conductivity-temperature-depth (CTD) data taken near the receiving arrays, is shown in Figure 2.

Surface weather conditions included excellent visibility, clear skies, northerly winds of 0–10 knots, and a steady barometric pressure of 29.8 mm Hg. The air surface temperature dropped from 0 to −40°F during the day these measurements were made. Ice thickness was nominally 8 ft with scattered ridges from 30 to 50 ft deep. Further environmental details are available in Reference 3.

B. Data Acquisition System

Hydrophones with different sensitivities were used. Two pairs of hydrophones had preamp sensitivities that were 30 dB less than the other two pairs identified in Figure 1. The recording system gains were adjusted to yield approximately the same input voltage levels (±2.0 V) for all phones. The different sensitivities do not affect the calculated coherence.

The data acquisition system consists of an 18-channel signal conditioner, an 18-channel expanded video cassette recorder system (EVCR), a portable VHS video cassette recorder (VCR), and a time-code generator/reader. The signal conditioner prewhitens the analog signals from the hydrophones. The 18-channel EVCR digitizes and formats the signals and then records them on a standard VCR.[4] The signal conditioner includes a programmable synthesizer to generate calibration tones that are recorded at the beginning of each VCR tape. The EVCR also has low-pass filters, a multiplexer, a 12-bit analog-to-digital (A/D) converter, an error correction encoder, and a video formatter. The analog

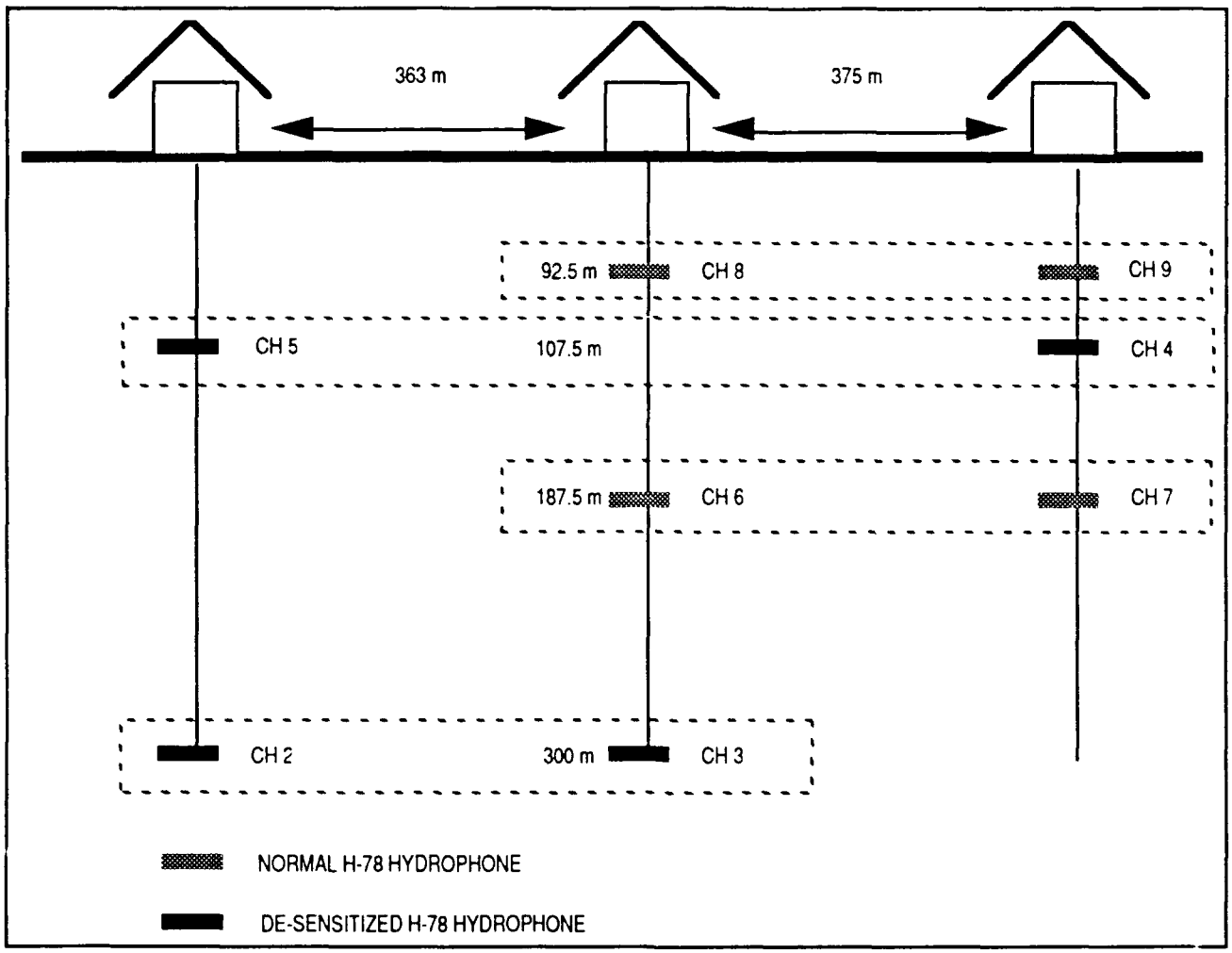

Figure 1. Experimental geometry identifying hydrophone pair depths, horizontal separations, and channels.

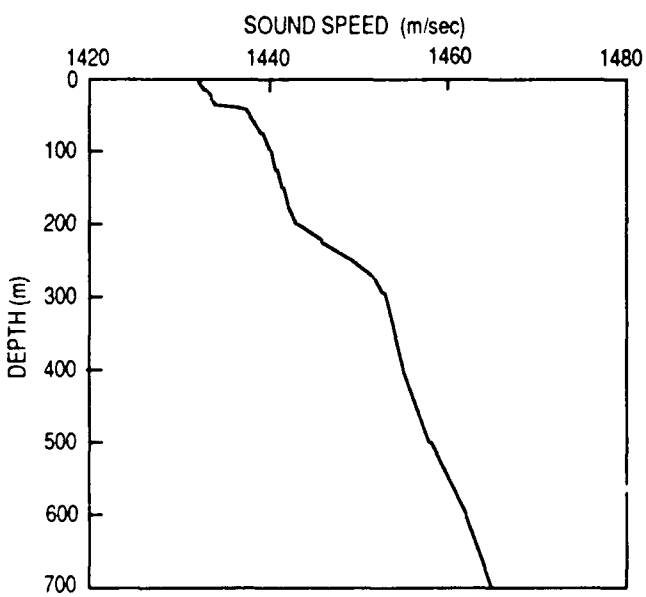

Figure 2. Sound speed profile derived from CTD measurements near the receiving array.

input/output for the EVCR is ±2 V peak-to-peak and the maximum single-channel sample rate is 4.4 kHz per channel. The two VCR audio channels are used for voice annotation and to record time code.

III. Data Processing

A. Digitizing

VCR tapes are played back through the EVCR, and the output analog signals are digitized at a 4000-Hz sampling rate using a computer-based, multichannel data acquisition system. This system includes 3-Mbyte random-access memory, a streaming 9-track tape drive, and a 474-Mbyte hard disk. It employs a 256-channel multiplexer with a 12-bit A/D converter. The amplitude is in digitized integers and is converted to voltage by 4.88 mV

per A/D unit. This circuitry does not employ a sample-and-hold and thu igitizes each channel sequentially. This time it across channels is corrected in subsequent processing. The digitized time series data are stored, along with a digitized 100-Hz synthesized reference tone, on 9-track magnetic tape and then processed on a VAX-11/750 computer.

B. Coherence Estimation

The hydrophone time series data are time-gated to separate the direct and surface-reflected arrivals for each shot. These arrivals were processed separately to estimate coherence for each hydrophone pair shown in Figure 1. The time series for each arrival were time-aligned to remove any effects due to array deformation and difference in acoustic path length. The time-aligned data are analyzed using the program published by Carter and Ferrie,[5] modified to incorporate different averaging schemes (discussed later).

Each time series is Hann-weighted and zero-padded, and the spectral estimates are computed from the Fourier transform. The Hann window is applied to the transient time series in an effort to reduce leakage between adjacent frequency bins due to sharp amplitude changes in the transient time series. Each data channel is aligned in the same location under the Hann window by using correlation and smoothed coherence transform (SCOT) functions to time align the two channels. Data at both ends of the resulting spectrum (0–100 Hz and 1200–2000 Hz) are dropped from further analysis. The mean-squared coherence, auto correlations, and cross correlations are also computed from these estimates. Figure 3 is a processing flow chart used for hydrophone time series pairs. This standard spectral analysis assumes that each hydrophone time series is a measure of a zero-mean stochastic process that is jointly stationary and ergodic. Values averaged just prior to the shot arrival are subtracted from the time series to provide zero-mean data.

Explosive data are not stationary, and ensemble averaging should be used to estimate the coherence. Since ensemble averaging is not possible, and since the mean and variance of the shots are not time independent, frequency band averaging[6] is employed to compute coherence.

The value of the coherence estimate is also dependent on the averaging bandwidth: the smaller the bandwidth, the higher the coherence estimate; the larger the bandwidth, the smaller the estimate. The spectrums shown here are averaged in the frequency domain in one-octave bands. Since the coherence value is depende on processing, this may not be a good estimate of true continuous wave coherence; i.e., a measure of the upper limit of common power between two channels at a given frequency, bu it can be used as a quantitative measure of similarity between the two signals.

Consistent processing is extremely important in order to compare results from different shots. Time windowing and, most importantly, averaging must be the same for each shot. A trade-off exists when employing spectral averaging. To obtain good estimates of spectrum levels and thus coherence, many degrees of freedom (number of FFT bins used in frequency averaging) are desired in the spectral averaging. This is important because of the high variability in the shot spectrum. However, to observe coherence variations with frequency, it is de d to average o fewer frequency bins. Also a - octave freq y averaging window represents fewer degree freedom for low frequencies than for higher frequencies. The data are presented for 3 one-octave bands (100–200 Hz, 200–400 Hz, 400–800 Hz) and 1 one-half-octave band (800–1200 Hz). The coherence variation in the half-octave band may be slightly higher because of the fewer degrees of freedom used in the frequency averaging.

Each direct arrival was processed using 250 points in the time series. Because of the time spread of the surface-reflected arrival, the time series was extended to 512 points. The autospectral estimations of the time series from each hydrophone, $G_{xx}(f)$ and $G_{yy}(f)$ and the cross spectral estimate, $G_{xy}(f)$, are averaged in the 3 one-octave bands to compute the magnitude-squared coherence (MSC) using Equation 1.

$$\gamma(f) = \frac{|\overline{G_{xy}(f)}|^2}{|\overline{G_{xx}(f)}|\ |\overline{G_{yy}(f)}|} . \qquad (1)$$

Phase difference as a function of frequency and estimates of the auto- and cross-correlation functions are computed and used in data analysis and quality assurance. Any hydrophone data pair in which the autocorrelations differ significantly are discarded from further analysis. Also computed is a smooth coherence transform (SCOT) function, which has

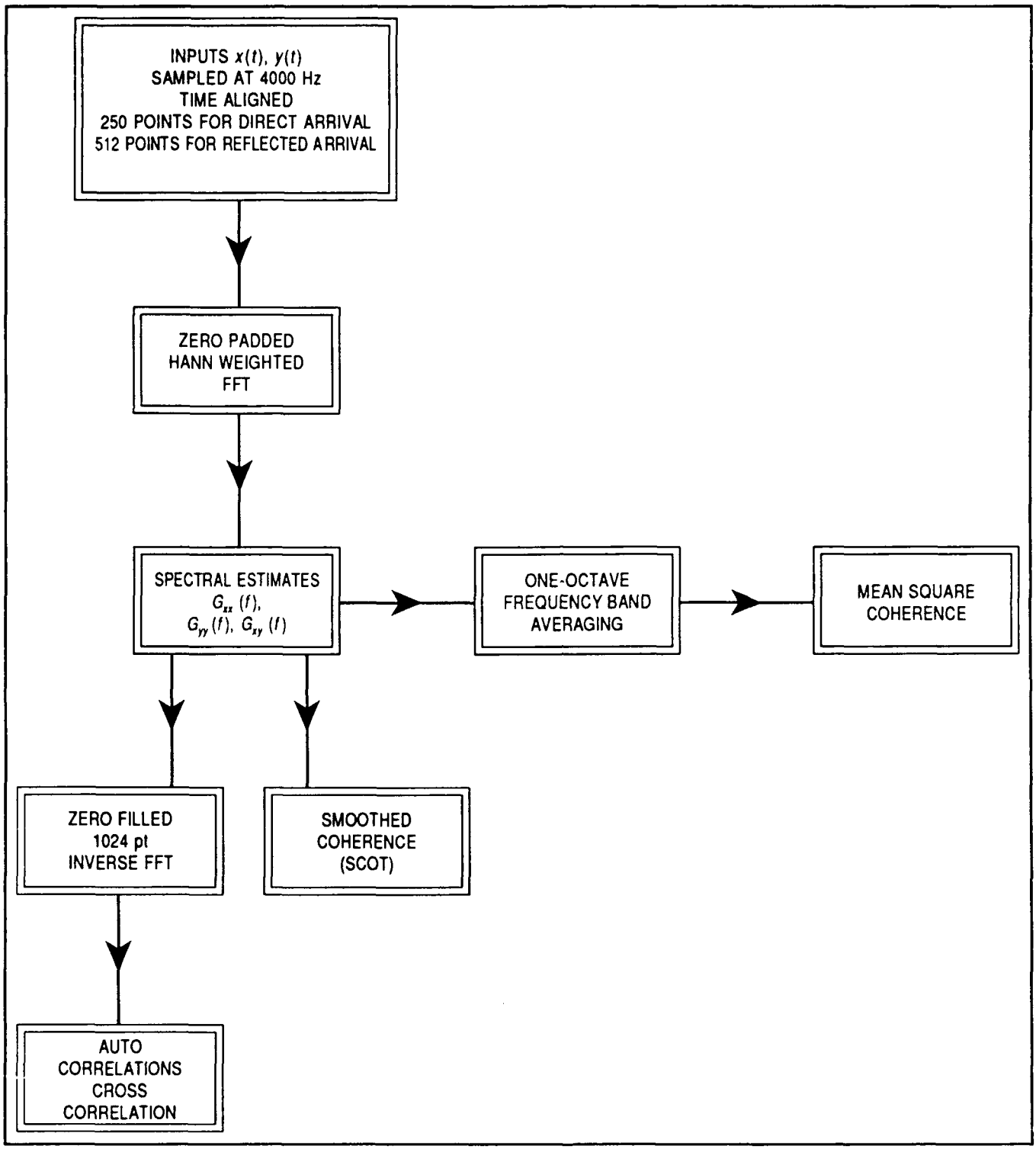

Figure 3. Data processing flow chart. The direct and single ice-reflected arrival are time-gated and processed separately.

been used to measure time delays between weak, broadband-correlated signals.[7,8] SCOT appears to give sharper time resolution of the cross correlation than the standard cross correlation. SCOT is useful to verify that any time delay between the two channels has been removed and to align both channels equally under the Hann window. SCOT is the Fourier transform of the smoothed complex coherence (i.e., the square root of the MSC) and is given as

$$\int_{-\infty}^{\infty} W(f)\gamma(f)e^{i2\pi\tau f}\,df\ , \qquad (2)$$

where $W(f)$ is the smoothed cosine weighting function, $\gamma(f)$ is the complex coherence as a function of frequency, f is frequency, and τ is time lag.

IV. Broadband Acoustic Sources

A. Underwater Explosives

Underwater explosives have been used for many years in both naval and seismic research, and the received signals from these sources have been well studied.[9,10,11] Figure 4 shows the characteristic time series and spectrum for a shot at close range (193 m). The initial pressure peak is followed by several bubble pulse oscillations that diminish with time. These waveforms have a characteristic spectrum because of the interference between the initial shock impulse and subsequent bubble pulses. The result is range-dependent modulations between adjacent spectral peaks and deep nulls. Bubble pulse fundamental period and spectrum source levels are sensitive to the detonation depth and charge weight. If both the latter are known, then the pressure-time history of the idealized bubble pulse can be determined from Equation 3.[10]

Here, P is pressure in pounds per square inch, W is the charge weight in pounds, R is the slant range in feet, T is time in seconds, and Z is the explosion depth in feet, plus 33. All of the SUS charges used have an equivalent TNT charge weight of 6 oz and a nominal detonation depth of 1000 ft ± 100 ft (320 m ± 32 m). Bubble pulse migration is negligible for this small charge weight.

By measuring the time from launch to detonation and the time between the surface and bottom arrivals at the hydrophone detonation depth, calibration was accomplished using 17 SUS charges. The average detonation depth was 965 ft (310 m) with a standard deviation of 41 ft (13 m).

The pressure-time histories for both the calibration data (represented in Fig. 4) and the long-range direct arrival agree with the time history predicted by Equation 3. The measured values of T_b from the calibration data show some variability associated with detonation depth variability and digitizing rate error (0.00025 seconds). The predicted time for T_b from Equation 3 is 0.0096, and the average measured value from the calibration shots is 0.0089 seconds. These values give predicted and measured bubble pulse frequencies of 104 and 113 Hz, respectively.

Interference between the initial shock peak and the bubble pulses causes the deep nulls that characterize the shot spectrum in Figure 4. The energy rises sharply at low frequencies, peaks near the bubble pulse frequency, and falls off at approximately 6 dB per octave, as predicted for exponential waves. The lower frequencies are dominated by the bubble pulse fundamental and higher frequencies by the shock wave. Secondary bubble pulses introduce weaker interference patterns,

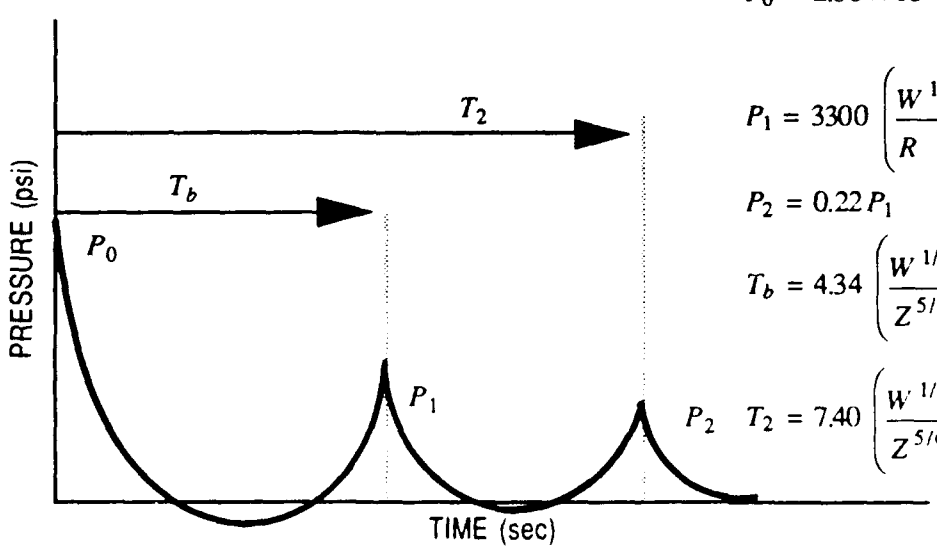

$$P_0 = 2.08 \times 10^4 \left(\frac{W^{1/3}}{R}\right)^{1.13}$$

$$P_1 = 3300 \left(\frac{W^{1/3}}{R}\right)$$

$$P_2 = 0.22 P_1$$

$$T_b = 4.34 \left(\frac{W^{1/3}}{Z^{5/6}}\right)$$

$$T_2 = 7.40 \left(\frac{W^{1/3}}{Z^{5/6}}\right) \qquad (3)$$

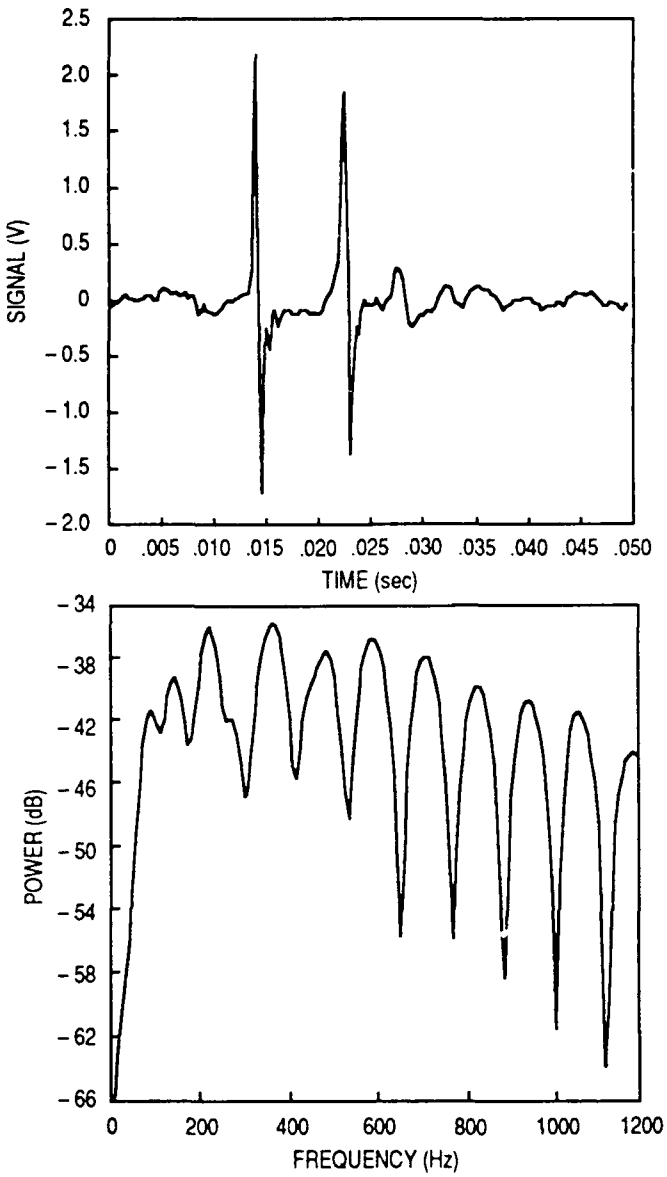

Figure 4. Typical explosive shot time series and spectrum at close range (193 m).

causing peak and null frequency shifts at higher frequencies. The null spacing is equal to the bubble pulse frequency.

B. Time Series and Spectrum Analysis

Ray trace results for the deepest hydrophone pair appear in Figure 5. All predicted times between the direct, ice-reflected, and bottom-reflected arrivals showed reasonable agreement with the data for all ranges. The ray trace also shows the half-channel effect because of the sound speed profile.

Figure 6 shows example acoustic signals from the deepest hydrophone pair corresponding to the direct arrival for a shot at a range of 3 km. Figure 6a is the time series data for each channel; 6b is the narrowband spectral estimate for each channel; 6c is the autocorrelation for each channel; 6d is the narrowband cross-spectral estimate; 6e shows the cross correlation between channels; 6f is the phase difference between channels as a function of frequency; 6g shows the SCOT correlation; and 6h is the mean-square coherence obtained from one-octave-band averaging of the spectal estimates. Figure 7 shows corresponding results for the ice-reflected arrival in the same format and for the same shot as in Figure 6.

The time series in Figure 6a is an interference pattern created by the initial explosive pressure pulse and subsequent pulses from bubble oscillation. In the example shown here, the two received pulses show the same general shape; however, in channel 2 (the left channel), the duration of the received signal is shorter than in channel 3 (the right). The first two peaks align very well, but the last peak occurs 5 msec later in the right pulse than in the left pulse. This 5-msec delay is common for other shots and for other hydrophone pairs in this data set, but cannot be adequately explained. The time is too short to be an effect of internal waves. Volume inhomogeneity is also unlikely, and ocean micro-structure is generally associated with amplitude fluctuations—not time spreading. One possible source might be micro-multipaths that are always present but are even more prolific near the half-channel boundary created by the sound speed profile. When this occurs the time alignment is always based on the first arrivals.

The time series for the ice-reflected arrival (Fig. 7a) shows a much stronger interference pattern than the direct arrival. This time series also exhibits noticeable time spreading due to under-ice scattering. The ice-reflected time series is over twice as long as the direct arrival and was truncated to 512 points for spectrum estimation and analysis.

The spectra from the long-range direct and reflected arrivals (Figs. 6 and 7) maintain the characteristic short-range shot spectrum shown in Figure 4. The narrowband peaks and nulls in the spectra will shift and vary in level because of interference among the initial shock pulse and subsequent bubble pulses. The reflected arrival spectra exhibit even stronger interference effects on the levels and locations of the peaks and nulls. Also, the characteristic 6 dB per octave roll-off appears to be shifted to slightly higher frequencies.

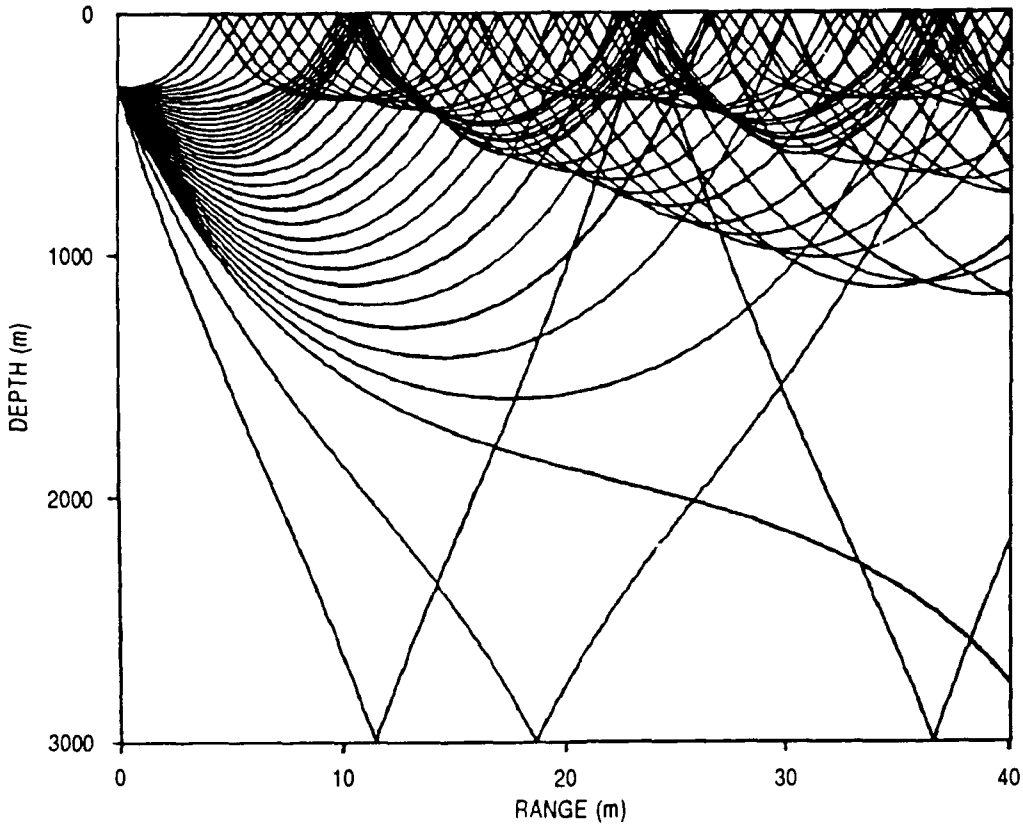

Figure 5. Ray trace based on sound speed profile from Figure 2.

As expected, the autocorrelations of the direct and reflected arrivals (Figs. 6c and 7c) exhibit secondary peaks that corresponds to multiples of the fundamental bubble pulse frequency. The ice-reflected autocorrelation shows a slightly longer correlation time because of the scattering of the reflected waveform. The phase difference plots (Figs. 6f and 7f) show that the phase changes between the two channels are random and that there is no common mode interference. The cross-correlation and SCOT functions (Figs. 6e, 6g, 7e, 7g) verify that only the waveforms of the two arrivals are being compared in the coherence estimate and that there is no time delay between channels to modulate the cross spectra.

V. Coherence Estimates

A. Direct and Ice-Reflected Arrivals

The coherence for the direct and ice-reflected arrivals are shown in Figures 6h and 7h. Figures 8–11 summarize the coherence data for the direct and ice-reflected arrivals in the four frequency bands as a function of horizontal range for the hydrophone pairs identified in Figure 1. Note that the ranges are not equally spaced. Substantial variability with range and frequency can be seen in these figures. In general, the coherence values decrease with frequency for both arrivals. The noticeable exception is for the deepest hydrophone pair (Fig. 8), where the coherence increases with frequency for both arrivals.

For coherence to increase with frequency, the changes in phase difference between the two channels must decrease as frequency increases; i.e., the variability in the spectra (G_{xy}, G_{xx}, and G_{yy}) must diminish as frequency increases. In general, variability in the spectral levels shown in Figures 6b, 6d, 6f, 7b, 7d, and 7f does not diminish with increasing frequency. Although the direct arrival shows less change in the phase difference than the reflected arrival, there are no obvious smoothing trends with frequency for any arrival to explain the increasing coherence trend for higher frequencies.

B. Background Noise Coherence

The sound speed profile (Fig. 2) supports two half-channels at approximately 50 and 270 m. Time-pressure signals received at each hydrophone consists of two parts, the highly coherent contribution from

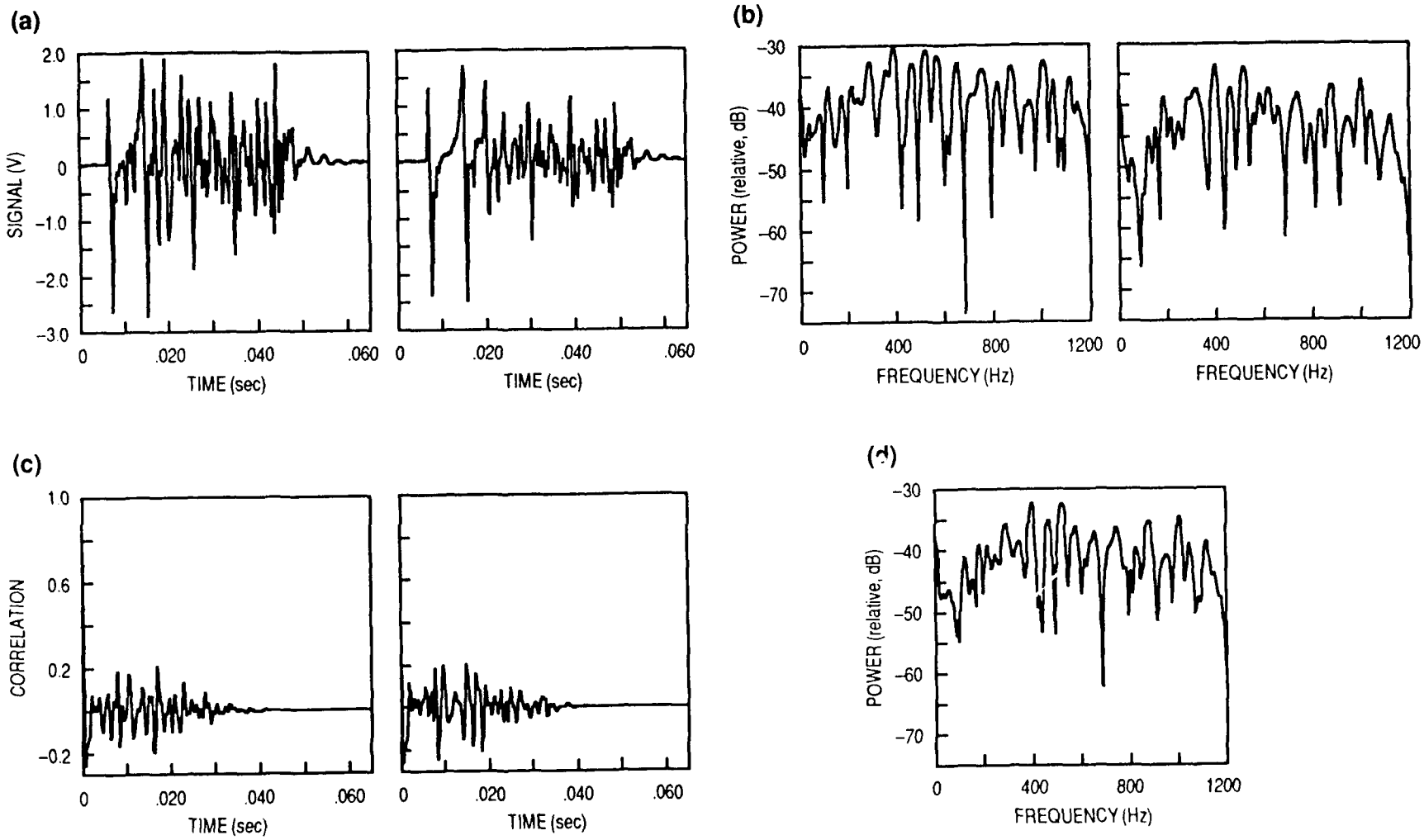

Figure 6. Typical results for the direct arrival at a horizontal of 2.7 km from the deepest hydrophone pair. (a) Time series for both channels. (b) the frequency spectrum for both channels, (c) the auto correlation for both channels, and (d) the cross spectrum.

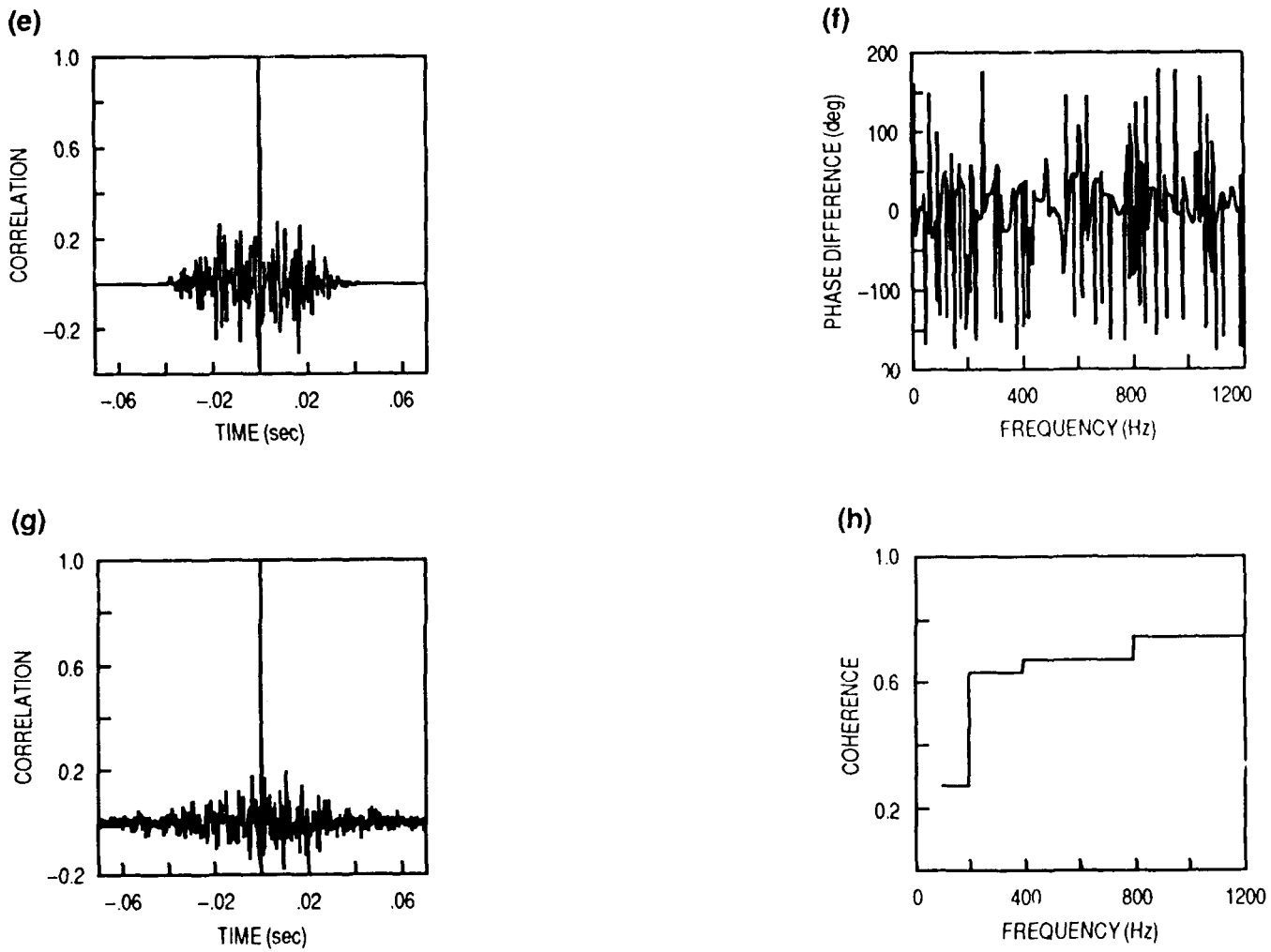

Figure 6 (cont.). (e) The cross correlation between channels, (f) the phase difference between channels, (g) the SCOT correlation, and (h) the computed MSC.

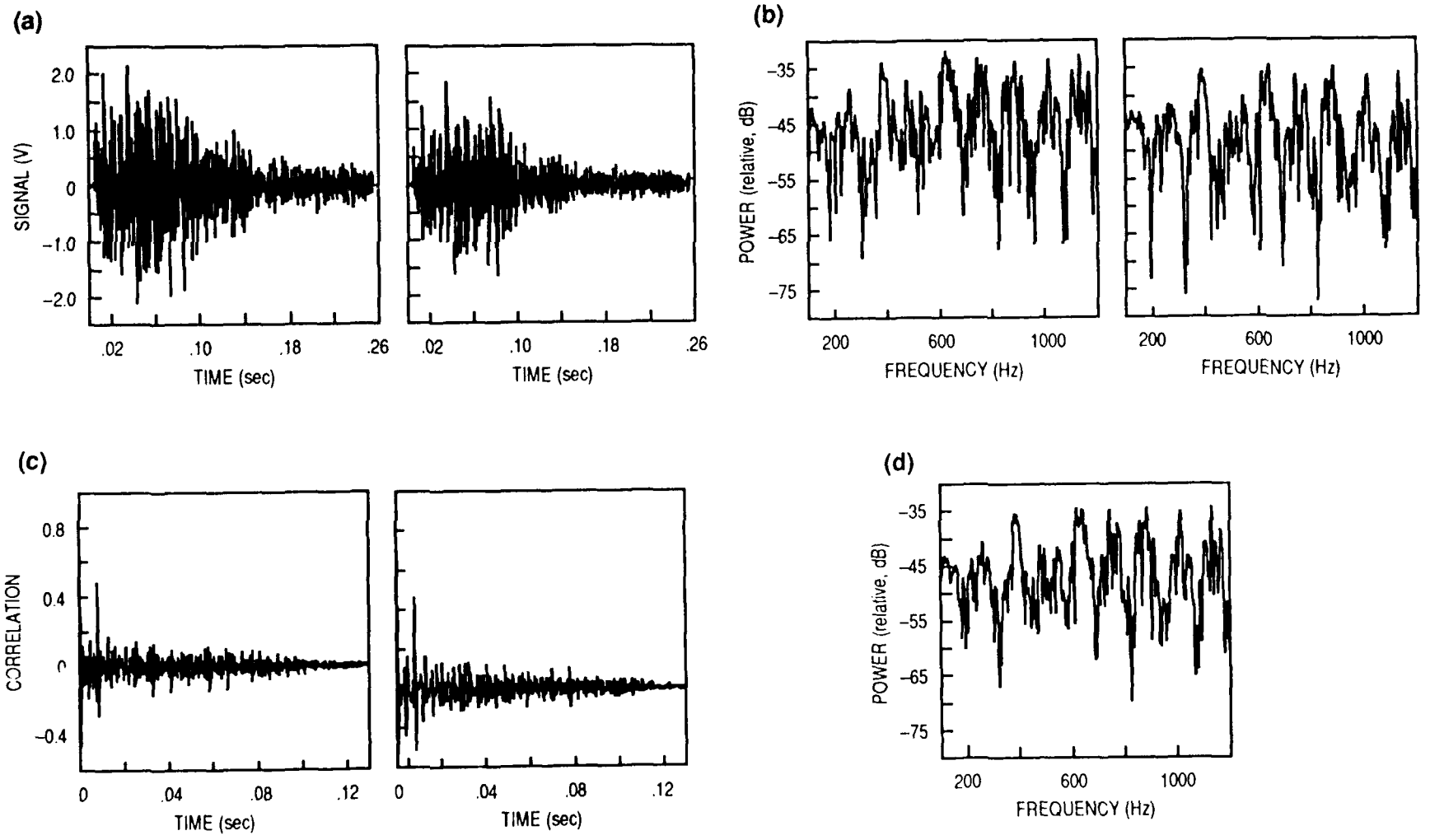

Figure 7. Typical results for the ice-reflected arrival and direct arrival at a horizontal of 2.7 km from the deepest hydrophone pair. (a) Time series for both channels, (b) the frequency spectrum for both channels, (c) the auto correlation for both channels, and (d) the cross spectrum.

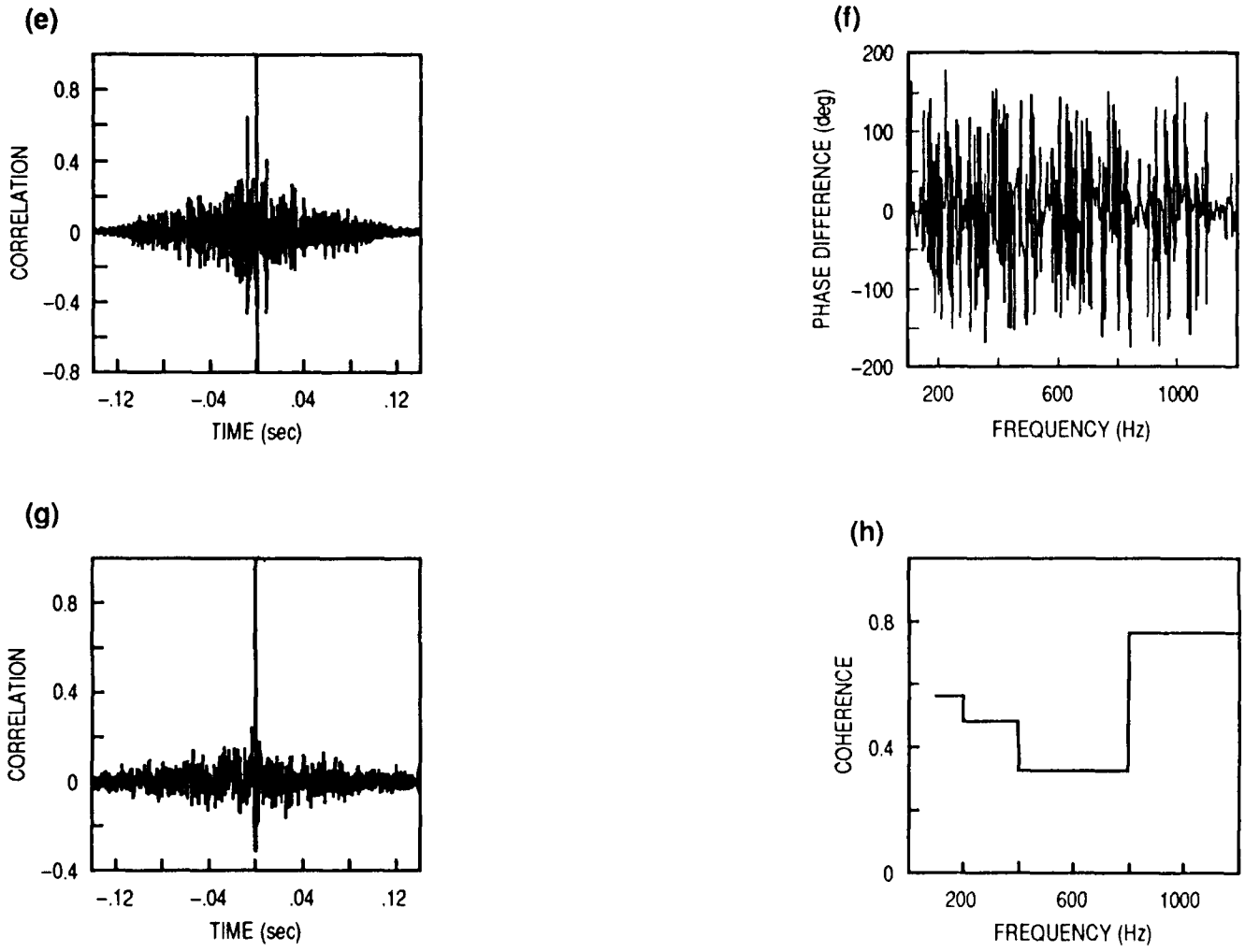

Figure 7 (cont.). (e) The cross correlation between channels, (f) the phase difference between channels, (g) the SCOT correlation, and (h) the computed MSC.

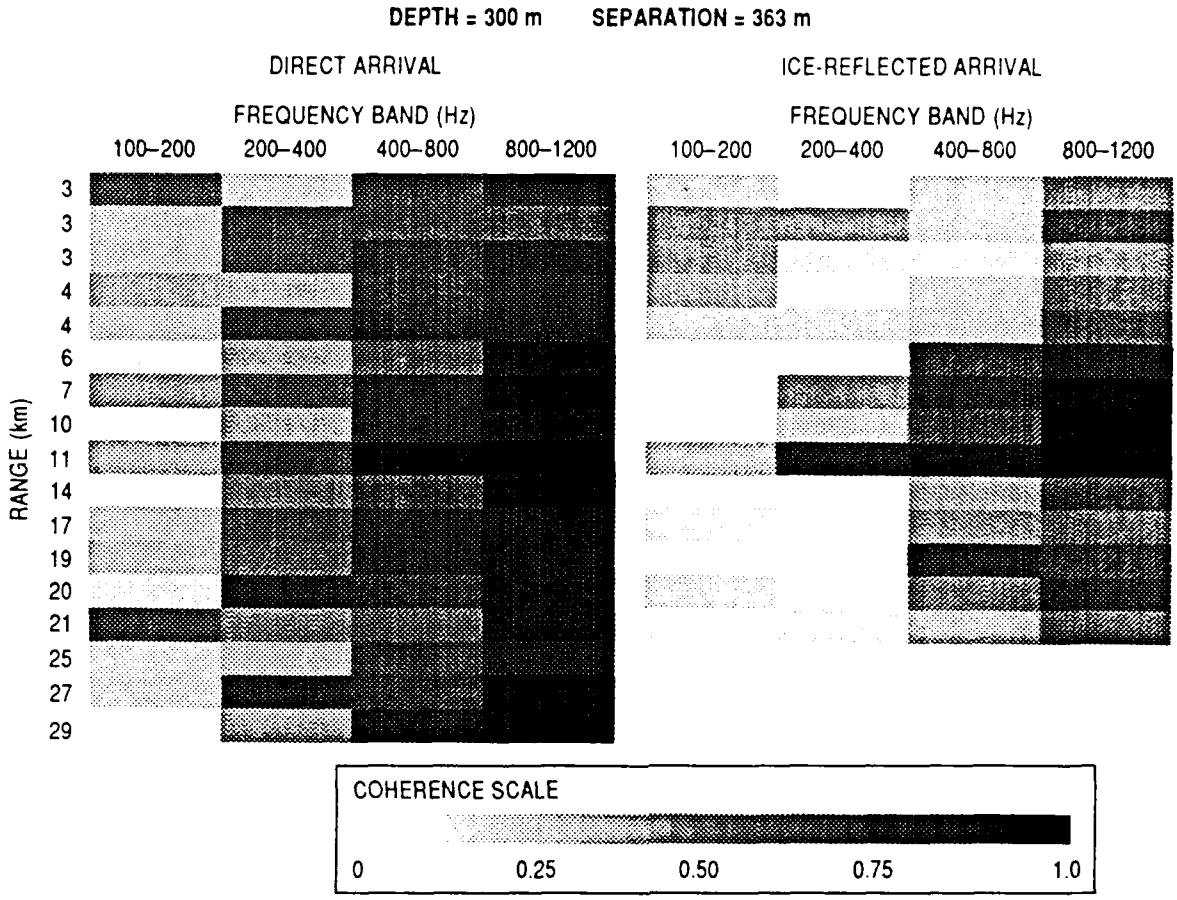

Figure 8. One-octave band averaged coherence estimates as a function of range for channels 2/3 as identified in Figure 1.

the shot and a smaller contribution from background noise. The main component of the background noise is ambient noise generated near the surface by ice cracking and movement, wind-blown ice and snow, and other mechanisms. Arctic ambient noise generated near the surface and other noise from long-range sources propagates farther inside the channels, but only local noise arriving from nearly vertical penetrates below the channel. Because of the presence of the acoustic half-channel, and because ambient noise originates near the surface, background noise coherence should be different above and below the half-channel. Inside the half-channel, noise from long-range sources is present; below the half-channel, primarily local noise sources contribute to the background noise. A noise time series was used to calculate the coherence of the background noise for hydrophone pairs inside and below the 270-m channel.

A noise time series of 250 points was taken prior to each shot arrival. This series was used to calculate the background noise coherence. The noise data were processed in the same manner as the direct arrival, except that no time alignment of the two channels was attempted. The noise coherence was computed using one-third-octave frequency band averaging to obtain a better defined frequency structure. Figure 12 shows the background noise coherence for the four hydrophone pairs as a function of the one-third octave band given for each SUS shot number in Table 1.

Inside the half-channel (data channels 4/5, 6/7, and 8/9) the noise coherence showed little or no linear frequency dependence for bands 6–12. Below the acoustic half-channel (data channels 2/3) the noise coherence decreased slightly with frequency for bands 6–12. Band 2 consistently had the highest noise coherence of any band for all hydrophone pairs, indicating noise coherence is greatest near 125 Hz. To examine frequency dependence, the background noise coherence data from Figure 12 were averaged over all SUS shots in each frequency band. Table 2 shows these averages and the standard deviation.

The averaged noise coherence shows similar frequency variability for the hydrophone pairs inside

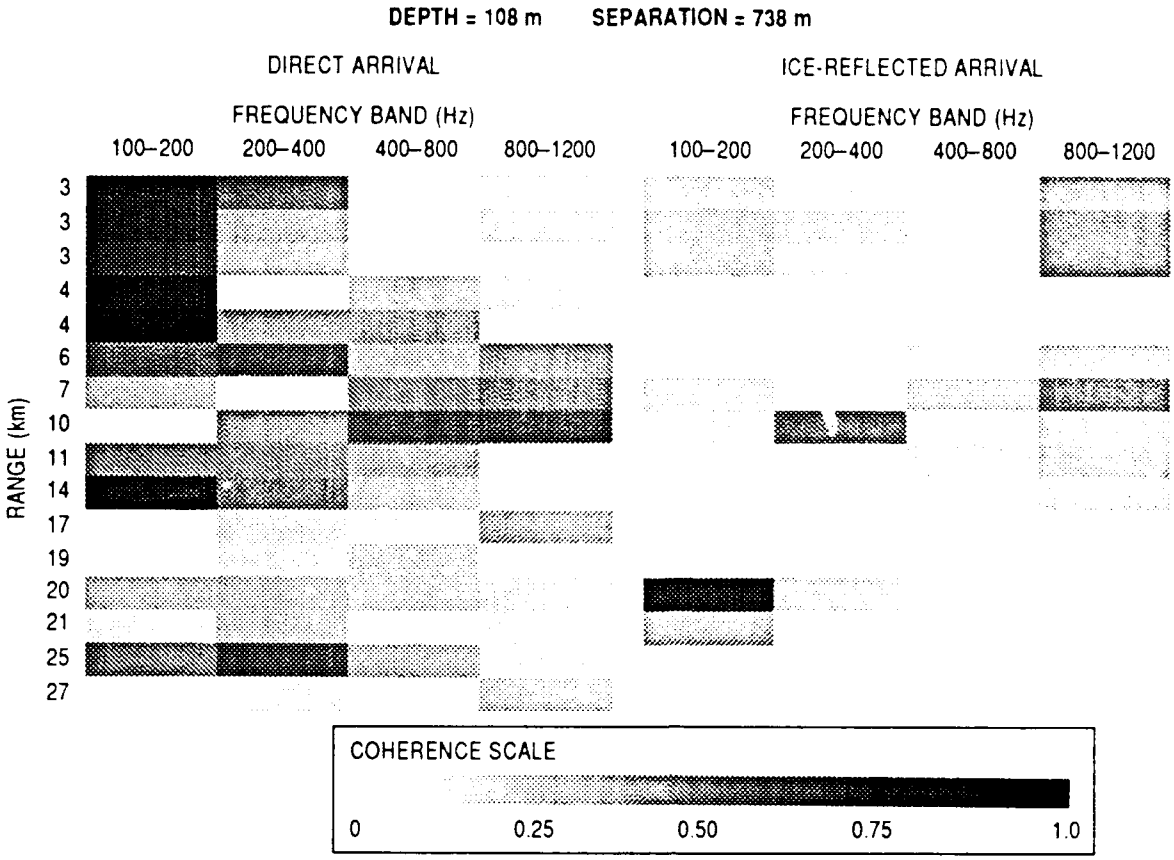

Figure 9. One-octave band averaged coherence estimates as a function of range for channels 4/5 as identified in Figure 1.

Table 1. Ambient noise coherence frequency bands shown in Figure 12.

BAND NUMBER	PASSBAND FREQUENCIES
1	89 – 112 Hz
2	112 – 141
3	141 – 178
4	178 – 224
5	224 – 282
6	282 – 355
7	355 – 447
8	447 – 562
9	562 – 708
10	708 – 891
11	891 – 1120
12	1120 – 1410

he half-channel (chs. 4/5, 6/7, and 8/9). Below the ıcoustic half-channel (ch. 2/3) the average noise :oherence shows a constant decrease with frequency. The standard deviation in Table 2 is fairly uniform and constant for all hydrophone pairs in the frequency bands 6–12. Thus, the decrease of noise coherence with frequency for the deep hydrophone pair is not a result of the number of FFT bins used in spectrum averaging. The standard deviation is higher in bands 1–5 because of fewer FFT bins for spectrum averaging. Band 2 consistently contains the highest noise coherence for all hydrophone pairs and corresponds to 125 Hz. The presence of a coherent background noise degrades the coherence of the shot signal received at the hydrophones. Inside the half-channel the degradation is frequency independent. Below the half-channel the degradation is slightly less at higher frequencies, causing the observed shot signal coherence increase with frequency.

The magnitude of coherence for the direct arrival is higher inside the half-channel than below the channel. The ice-reflected arrival undergoes attenuation and scattering due to reflection; thus, coherence is reduced inside the channel. Below the channel, the ambient noise coherence decreases, the reflected arrival penetrates because of steep reflection angles, and measured coherence increases.

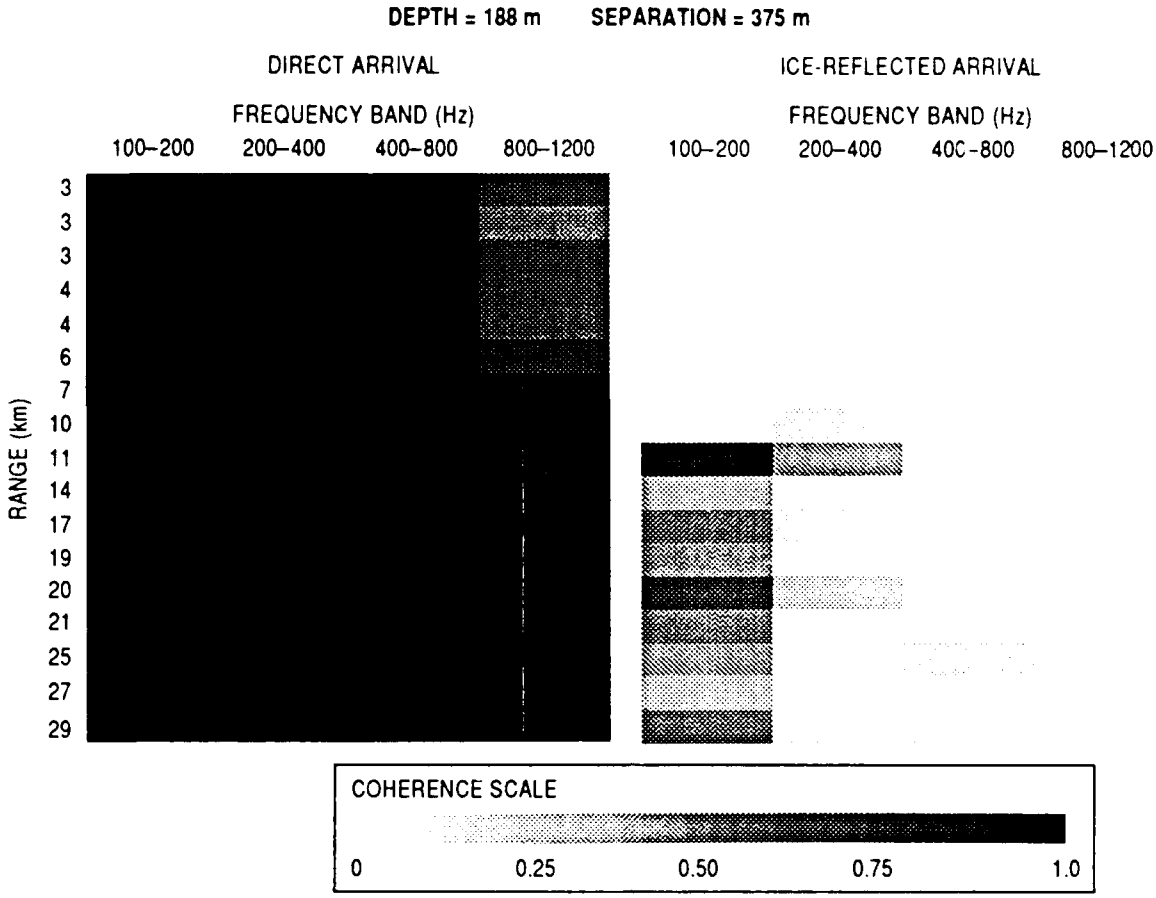

Figure 10. One-octave band averaged coherence estimates as a function of range for channels 6/7 as identified in Figure 1.

Table 2. Computed coherence averaged over all shots and standard deviation for each one-third octave band defined in Table 1 and for the hydrophone pairs identified in Figure 1.

AVERAGE	1	2	3	4	5	6	7	8	9	10	11	12
Channel 2/3	0.32	0.41	0.33	0.23	0.17	0.23	0.24	0.18	0.18	0.17	0.15	0.15
Channel 4/5	0.29	0.37	0.24	0.18	0.20	0.23	0.23	0.20	0.31	0.27	0.21	0.23
Channel 6/7	0.20	0.46	0.35	0.20	0.18	0.31	0.16	0.30	0.45	0.31	0.20	0.19
Channel 8/9	0.28	0.43	0.37	0.28	0.27	0.20	0.21	0.15	0.31	0.22	0.22	0.12
STD. DEV.	**1**	**2**	**3**	**4**	**5**	**6**	**7**	**8**	**9**	**10**	**11**	**12**
Channel 2/3	0.19	0.27	0.27	0.18	0.15	0.18	0.17	0.14	0.14	0.14	0.16	0.19
Channel 4/5	0.24	0.24	0.24	0.15	0.12	0.19	0.13	0.16	0.18	0.11	0.15	0.10
Channel 6/7	0.24	0.21	0.26	0.18	0.13	0.24	0.13	0.13	0.15	0.16	0.11	0.10
Channel 8/9	0.20	0.30	0.23	0.16	0.24	0.19	0.18	0.14	0.18	0.13	0.13	0.10

C. Horizontal Separation and Spatial Coherence

Data in Figure 9 were obtained with a horizontal sensor separation nearly double the others. Compared with Figure 11, it appears that doubling horizontal separation decreases coherence by half for the direct arrival. This effect for the ice-reflected arrival seems less, but there is insufficient data at other depths and separations to be conclusive. The ice-reflected arrival for the widely separated pair shows less frequency dependence than the direct arrival and slightly higher coherence than the same frequency bands for the smaller separation. Coherence changes in range appear in both the direct and reflected

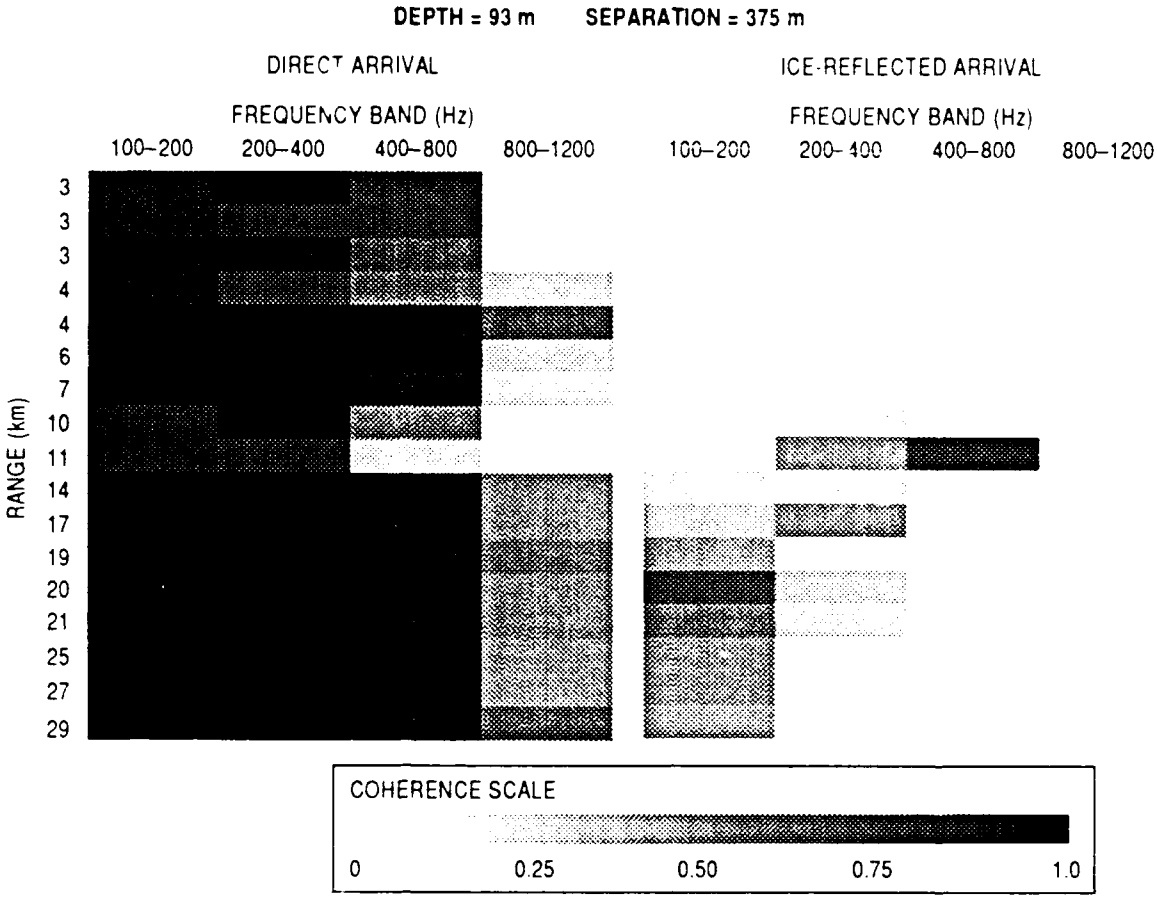

Figure 11. One-octave band averaged coherence estimates as a function of range for channels 8/9 as identified in Figure 1.

arrivals and increase slightly near 11 and 20 km. The ray trace (Fig. 5) also indicates an increase in amplitude near these ranges.

VI. Coherence Change After Reflection

Figure 13 shows the fractional change in coherence after a single under-ice reflection for the four frequency bands. The fractional change is

$$\left| \left(\gamma^2_{\text{direct}} - \gamma^2_{\text{reflected}} \right) / \gamma^2_{\text{direct}} \right|_R , \qquad (4)$$

where the bars denote an average over range (all shots) and γ^2 is the MSC. The change for pairs 6/7 and 8/9 are twice as great, on average, as for the deep pair, 2/3, and the wide pair, 4/5. No obvious depth dependencies are discernible, but the data do show a frequency trend. The lowest frequency band clearly shows the smallest fractional change in coherence.

The reflected arrival coherence is higher (i.e., negative change) than the direct arrival in the lowest frequency band in pair 2/3 and in the highest frequency band in pair 4/5. Pair 2/3 is the deepest pair (below the half-channel), and 4/5 has the greatest horizontal separation. Figure 14 shows the coefficient of variation (standard deviation/average) of the change in coherence over range. Variation is also highest for the deepest hydrophone pair and for the pair with the widest separation.

The change in coherence due to reflection is smaller for the low octave because low frequencies "see" a smoother surface and therefore less coherence loss because of scattering.

VII. Summary

Measurements were made of direct and ice-reflected arrivals from explosive acoustic sources under the Arctic ice pack. Coherence estimation is a difficult problem and is not defined theoretically

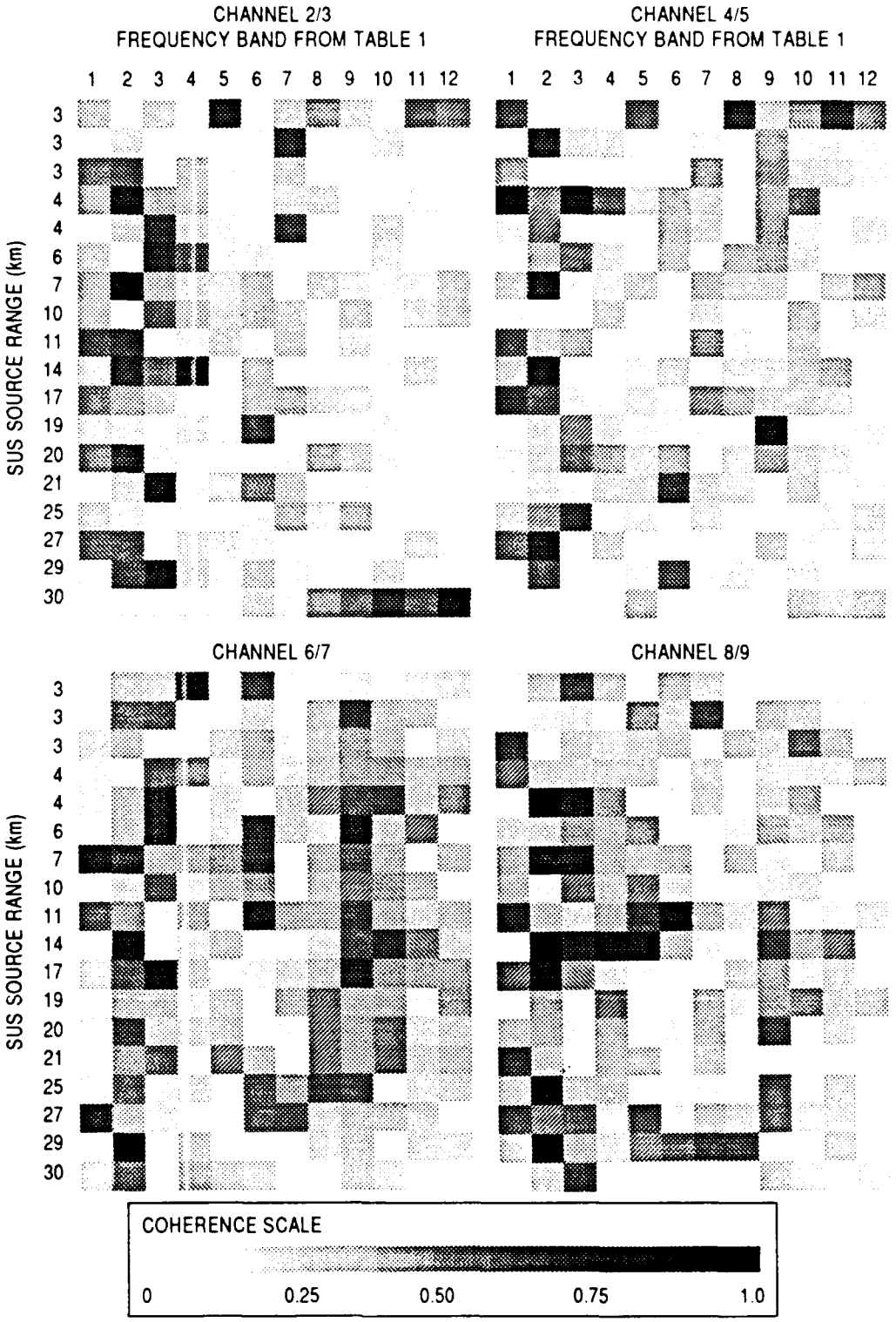

Figure 12. Background noise coherence estimates at the receiving hydrophones just prior to the arrival of the shot from the stated range. The hydrophone pairs are identified in Fig. 1.

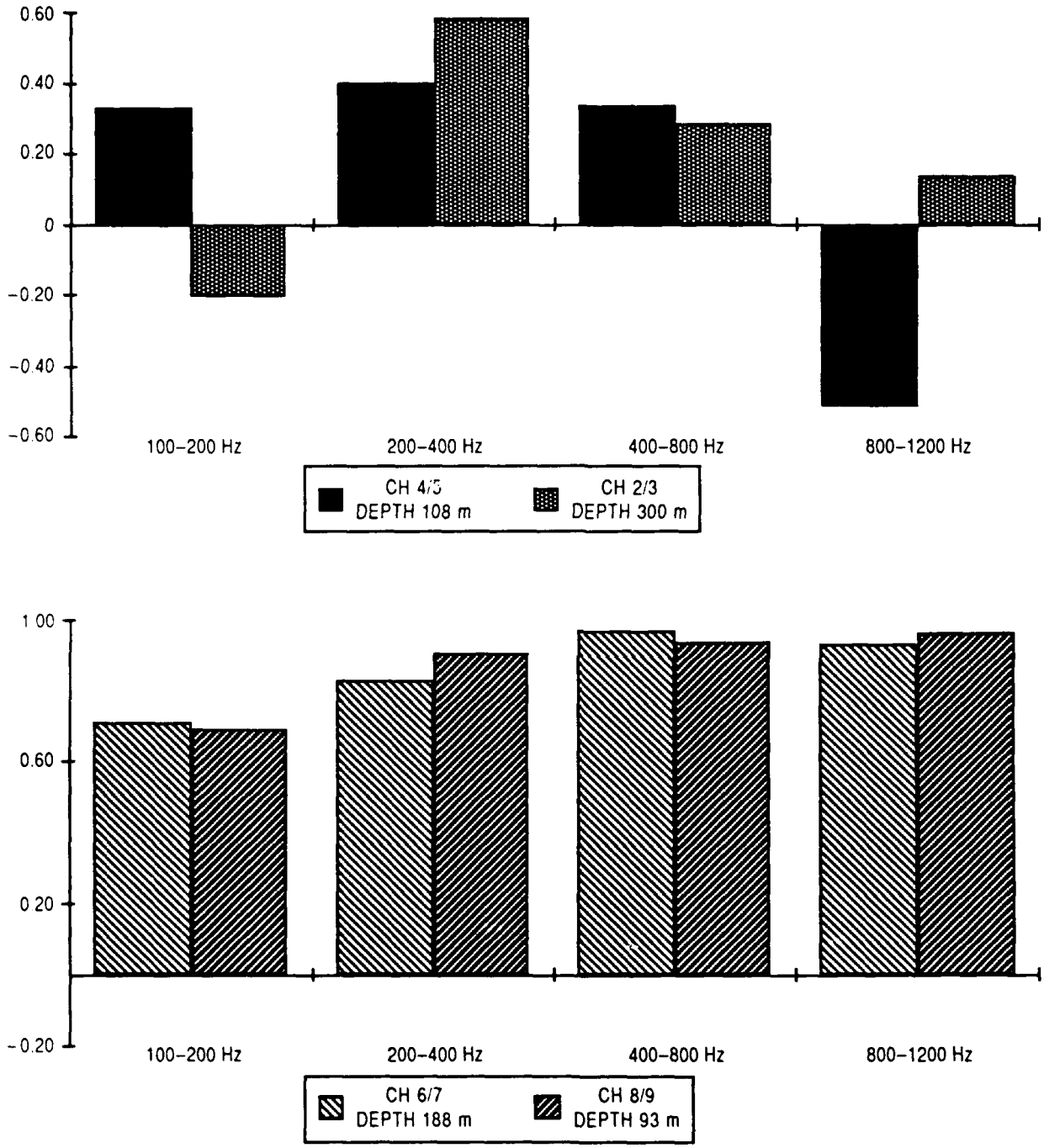

Figure 13. Range-averaged fractional change in coherence computed from Equation 4 after a single under-ice reflection.

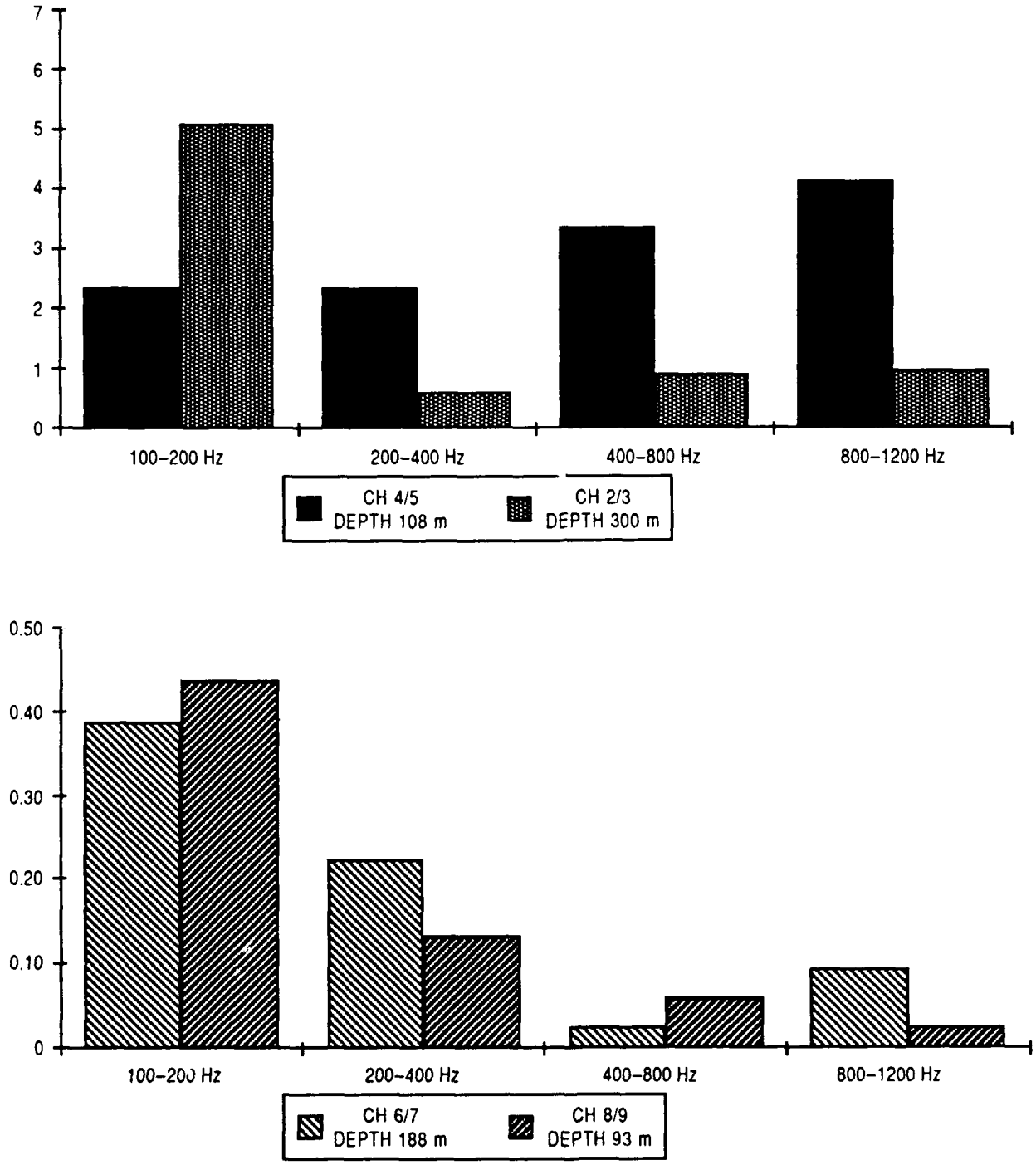

Figure 14. Range-averaged coefficient of variation (standard deviation/average) of fractional change.

for transient broadband signals. Horizontal coherence was found to be highly variable and dependent on the frequency-averaging bandwidth. One-octave frequency band averaging was chosen as an acceptable trade-off between coherence estimation variability, bias, and frequency resolution. Depending on geometry and the half-channel thickness, the highest values of coherence did not necessarily occur in the lowest frequency band. Both direct and ice-reflected arrivals showed the same general spread of spatial coherence changes—up to 50%. Coherence is both frequency and depth dependent for both the direct and ice-reflected arrivals. Some of the frequency dependence is due to background noise coherence inside and below a half-channel. The under-ice reflection has the smallest change in coherence in the lowest octave frequency band, and the magnitude of the change may be from 20 to 80%. The fractional change in coherence after a single under-ice reflection showed no obvious trend for these small grazing angles.

VIII. References

1. Ramsdale, D. J. and J. W. Posey (1987). Understanding underwater acoustics under the ice canopy. *Sea Technology*: 22-28, July.

2. Naval Sea Systems Command (1975). Technical Manual: Description, Operation, and Launching Underwater Sound Signal Mark 123 Mod 0. NAVSEA OD 49903.

3. Garrison, G. T., T. Wen, and M. L. Welch (1985). Environmental Measurements in the Beaufort Sea, Autumn 1984. APL/UW, Seattle, Washington, March.

4. Horsley, L. and D. J. Ramsdale (1986). Performance evaluation of the expanded video cassette recording system (EVCR). *Proceedings of the Marine Data Systems International Symposium* 385–389, April 30–May 2.

5. Carter, G. C. and J. F. Ferrie (1979). A coherence and cross spectral estimation program. *Programs for Digital Signal Processing*, IEEE Acoustics, Speech, and Signal Processing Society

6. Otnes, R. K. and L. Enochson (1978). *Applied Time Series Analysis*. New York (NY): John Wiley and Sons, pp. 347–350.

7. Knapp, C. H. and G. C. Carter (1976). The generalized correlation method for estimation of time delay. *IEEE Transactions on Acoustics, Speech, and Signal Processing*, V. ASSP-24, No. 4.

8. Carter, G. C., A. H. Nuttall, and P. G. Cable (1972). The Smooth Coherence Transform (SCOT). NUSC Technical Memorandum TC-159-72.

9. Urick, R. J. (1983). *Principles of Underwater Sound*. Third Edition, New York (NY): McGraw-Hill, pp. 87–98.

10. Gaspin, J. B. and V. K. Shuler (1973). Source Levels of Shallow Underwater Explosions. Naval Ordnance Laboratory Report TR71-160, White Oak, Maryland.

11. Mitchell, S. K., N. R. Bedford, and M. S. Weinstien (1976). Determination of source depth from the spectra of small explosions observed at long ranges. *J. Acoust. Soc. Am.* 60: 4.

12. Eckart, C. (1953). The scattering of sound from the sea surface. *J. Acoust. Soc. Am.* 25: 566-570.

13. Clay, C. S. and H. Medwin (1977). *Acoustical Oceanography: Principles and Applications*. New York (NY): Wiley-Interscience, pp. 338–344.

14. Berkson, J. M. (1980). Measurements of coherence of sound reflected from ocean sediments. *J. Acoust. Soc. Am.* 68(5).

Distribution List

Applied Physics Laboratory
Johns Hopkins University
Johns Hopkins Road
Laurel MD 20707

Applied Physics Laboratory
University of Washington
1013 NE 40th St.
Seattle WA 98105

Applied Research Laboratory
Pennsylvania State University
P.O. Box 30
State College PA 16801-0030

Applied Research Laboratories
University of Texas at Austin
P.O. Box 8029
Austin TX 78713-8029

Assistant Secretary of the Navy
Research, Development & Acquisition
Navy Department
Washington DC 20350-1000

Chief of Naval Operations
Navy Department
Washington DC 20350-2000
Attn: OP-71
OP-987

Chief of Naval Operations
Oceanographer of the Navy
U.S. Naval Observatory
34th & Massachusetts Ave. NW
Washington DC 20392-1800
Attn: OP-096
OP-0961B

David W. Taylor Naval Research Center
Bethesda MD 20084-5000
Attn: Commander

Defense Mapping Agency
Systems Center
8613 Lee Hwy.
Mail Stop A-13
Fairfax VA 22031-2138
Attn: Code PRN

Fleet Antisub Warfare Tng Ctr-Atl
Naval Station
Norfolk VA 23511-6495
Attn: Commanding Officer

Fleet Numerical Oceanography Center
Monterey CA 93943-5005
Attn: Commanding Officer

National Ocean Data Center
1825 Connecticut Ave., NW
Universal Bldg. South, Rm. 206
Washington DC 20235

Naval Air Development Center
Warminster PA 18974-5000
Attn: Commander

Naval Air Systems Command HQ
Washington DC 20361-0001
Attn: Commander

Naval Civil Engineering Laboratory
Port Hueneme CA 93043
Attn: Commanding Officer

Naval Coastal Systems Center
Panama City FL 32407-5000
Attn: Commanding Officer

Naval Facilities Engineering
Command HQ
200 Stovall St.
Alexandria VA 22332-2300
Attn: Commander

Naval Oceanographic Office
Stennis Space Center MS 39522-5001
Attn: Commanding Officer
Technical Director, L. Bernard
Library

Naval Oceanography Command
Stennis Space Center MS 39529-5000
Attn: Commander

Naval Oceanographic & Atmospheric
Research Laboratory
Atmospheric Directorate
Monterey CA 93943-5006
Attn: Code 400

Naval Oceanographic & Atmospheric
Research Laboratory
Stennis Space Center MS 39529-5004
Attn: Code 100
Code 105
Code 115
Code 125L (10)
Code 125P
Code 200
Code 300

Naval Ocean Systems Center
San Diego CA 92152-5000
Attn: Commander

Naval Postgraduate School
Monterey CA 93943
Attn: Superintendent

Naval Research Laboratory
Washington DC 20375
Attn: Commanding Officer
Technical Director
Library (3)

Naval Sea Systems Command HQ
Washington DC 20362-5101
Attn: Commander

Naval Surface Warfare Center Det
Silver Spring
White Oak Laboratory
10901 New Hampshire Ave.
Silver Spring MD 20903-5000
Attn: Officer in Charge
Library

Naval Surface Warfare Center
Dahlgren VA 22448-5000
Attn: Commander

Naval Underwater Systems Center
Newport RI 02841-5047
Attn: Commander

Naval Underwater Systems Center Det
New London Laboratory
New London CT 06320
Attn: Officer in Charge

Office of Naval Research
800 N. Quincy St.
Arlington VA 22217-5000
Attn: Code 10D/10P, Dr. E. Silva
Code 112, Dr. E. Hartwig
Code 12
Code 10

Office of Naval Research
ONR European Office
PSC 802 Box 39
FPO AE 09499-0700
Attn: Commanding Officer

Office of Naval Technology
800 N. Quincy St.
Arlington VA 22217-5000
Attn: Code 20, Dr. P. Selwyn
Code 228, Dr. M. Briscoe
Code 228, CDR. L. Bounds
Code 22, Dr. T. Warfield

Scripps Institution of Oceanography
University of California
291 Rosecrans St.
San Diego CA 92106-3505

Space & Naval Warfare Sys Com
Director of Navy Laboratories
SPAWAR 005
Washington DC 20363-5100
Attn: Commander

Woods Hole Oceanographic Institution
P.O. Box 32
Woods Hole MA 02543
Attn: Director

REPORT DOCUMENTATION PAGE

Form Approved
OMB No. 0704-0188

Public reporting burden for this collection of information is estimated to average 1 hour per response, including the time for reviewing instructions, searching existing data sources, gathering and maintaining the data needed, and completing and reviewing the collection of information. Send comments regarding this burden estimate or any other aspect of this collection of information, including suggestions for reducing this burden, to Washington Headquarters Services, Directorate for Information Operations and Reports, 1215 Jefferson Davis Highway, Suite 1204, Arlington, VA 22202-4302, and to the Office of Management and Budget, Paperwork Reduction Project (0704-0188), Washington, DC 20503.

1. Agency Use Only *(Leave blank).*

2. Report Date.
January 1992

3. Report Type and Dates Covered.
Final

4. Title and Subtitle.
Under-Ice Broadband Transient Measurements and Processing

5. Funding Numbers.

Work Unit No	12421A
Program Element No	0602435N
Project No	RJ035
Task No	I21
Accession No	DN496433

6. Author(s).
Roger W. Meredith

7. Performing Organization Name(s) and Address(es).
Naval Oceanographic and Atmospheric Research Laboratory
Ocean Acoustics and Technology Directorate
Stennis Space Center, Mississippi 39529-5004

8. Performing Organization Report Number.
NOARL Report 15

9. Sponsoring/Monitoring Agency Name(s) and Address(es).
Naval Oceanographic and Atmospheric Research Laboratory
Ocean Acoustics and Technology
Stennis Space Center, Mississippi 39529-5004

10. Sponsoring/Monitoring Agency Report Number.

11. Supplementary Notes.

12a. Distribution/Availability Statement.
Approved for public release; distribution is unlimited. Naval Oceanographic and Atmospheric Research Laboratory, Stennis Space Center, Mississippi 39529-5004.

12b. Distribution Code.

13. Abstract *(Maximum 200 words).*

This report examines the horizontal spatial coherence of broadband acoustic energy in the frequency range 100-1200 Hz from explosive sources under the ice pack. The data were recorded on four hydrophone pairs with a nominal sensor separation of 370 m from source ranges from 3 to 25 km. Mean-square coherence is computed separately for the direct and ice-reflected propagation paths, and octave-band frequency averaging reduces variability inherent in the coherence estimation associated with explosive acoustic sources. Coherence varies significantly with sensor depth, range, and frequency. Background noise coherence is also examined briefly. Changes in coherence because of under-ice reflection are smallest for the 100-200 Hz octave band, but the change may be as high as 50% for the higher frequency bands.

14. Subject Terms.
sea ice, noise, Arctic Ocean, coherence, transients

15. Number of Pages.
22

16. Price Code.

17. Security Classification of Report.	18. Security Classification of This Page.	19. Security Classification of Abstract.	20. Limitation of Abstract.
Unclassified	Unclassified	Unclassified	Same as report